Journal of Hazardous Materials 456 (2023) 131643

Contents lists available at ScienceDirect

Journal of Hazardous Materials

journal homepage: www.elsevier.com/locate/jhazmat

Research Paper

Nanozyme colorimetric sensor array based on monatomic cobalt for the discrimination of sulfur-containing metal salts

Hongsu Wang [a], Fengling Wu [a], Lifang Wu [a], Jingqi Guan [b,*], Xiaodi Niu [a,*]

[a] College of Food Science and Engineering, Jilin University, Changchun 130062, PR China
[b] Institute of Physical Chemistry, College of Chemistry, Jilin University, 2519 Jiefang Road, Changchun 130021, PR China

HIGHLIGHTS

- A simple and effective colorimetric sensor array was constructed based on CoN_4-G.
- The barrierless electron interaction led to the higher oxidase activity of CoN_4-G.
- The array could generate a fingerprint to identify various SCMs by LDA analysis.
- The array gave low LODs for SCMs detection.
- A smartphone-based APP was constructed to promote the on-site detection of SCMs.

GRAPHICAL ABSTRACT

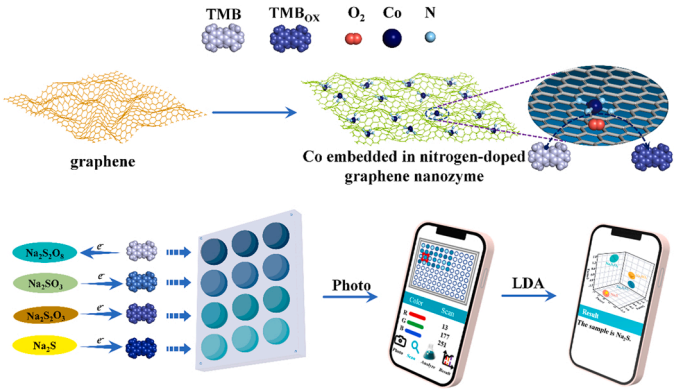

ARTICLE INFO

Editor: Lingxin Chen

Keywords:
Monatomic nanozymes
Sulfur-containing metal salts
Colorimetric sensor array
Smartphone

ABSTRACT

The identification of sulfur-containing metal salts (SCMs) is of great interest because they play an important role in many biological processes and diseases. Here, we constructed a ternary channel colorimetric sensor array to detect multiple SCMs simultaneously, relying on monatomic Co embedded in nitrogen-doped graphene nanozyme (CoN_4-G). Due to the unique structure, CoN_4-G exhibits activity similar to native oxidases, capable of catalysing directly the oxidization of 3,3′,5,5′-tetramethylbenzidine (TMB) by O_2 molecules independent of H_2O_2. Density functional theory (DFT) calculations suggest that CoN_4-G has no potential barrier in the whole reaction route, thus presenting higher oxidase-like catalytic activity. Based on different degrees of TMB oxidation, different colorimetric response changes are obtained as "fingerprints" on the sensor array. The sensor array can discriminate different concentrations of unitary, binary, ternary, and quaternary SCMs and has been successfully applied to detect six real samples (soil, milk, red wine and egg white). To advance the field detection of the above four types of SCMs, we creatively propose a smartphone-based autonomous detection platform with a linear range of 1.6–320 μM and a limit of detection of 0.0778–0.218 μM, which demonstrates the potential use of sensor arrays in the application of disease diagnosis and food and environment monitoring.

* Corresponding authors.
E-mail addresses: guanjq@jlu.edu.cn (J. Guan), niuxd@jlu.edu.cn (X. Niu).

https://doi.org/10.1016/j.jhazmat.2023.131643
Received 31 December 2022; Received in revised form 4 May 2023; Accepted 13 May 2023
Available online 14 May 2023

1. Introduction

Sulfur-containing metal salts (SCMs), such as sodium sulfide (Na_2S), sodium sulfite (Na_2SO_3), sodium thiosulfate ($Na_2S_2O_3$) and sodium persulfate ($Na_2S_2O_8$), pose potential risks to human health [1,22,6]. Excessive intake of SCMs may result in Alzheimer's, diabetes, liver cirrhosis, cancer and Down syndrome [3,33]. Therefore, the development of a reliable technology for the simultaneous detection of these SCMs is of great significance to food safety and human health. The current methods of detecting SCMs are mainly based on instrumental analysis, such as high-performance liquid chromatography [35] and the chemiluminescence probe method [25], both of which have high sensitivity and accuracy. However, they have drawbacks that greatly limit their application, including the need for wide technical personnel training, expensive laboratory instruments, high detection cost, complex sample pretreatment and long-time signal processing; therefore, they cannot meet the real-time analysis of large-scale samples. Furthermore, other methods have been established for rapid detection and quantification, such as fluorescence spectroscopy [9] and electrochemical analysis [20]. However, these methods have some disadvantages, such as the use of toxic organic compounds as the fluorescence source in the former method and the tedious electrode modification process in the latter method.

Owing to its simple operation, low cost and convenient signal readout, colorimetry has attracted wide attention [7,24]. However, the traditional colorimetric method, limited by the "lock-key" specific recognition mechanism, can only be used to detect or identify a single target substance. Hence, there is an urgent need to establish a rapid, stable and simple method for the synchronous determination of multiple substances in actual systems [4]. Strikingly, the colorimetric sensor array employs nonspecific recognition elements to generate a composite response pattern as a unique fingerprint for each target analyte by breaking the shackle of the "lock-key" specific recognition mechanism. In addition, the unique responses can be deeply differentiated using multivariate statistical methods, such as linear discriminant analysis (LDA) and principal component analysis (PCA), providing a general system for differentiating multiple analytes. In recent years, colorimetric sensing arrays have been widely applied in the fields of food quality detection [30], environmental protection [4], and disease diagnosis [18]. To date, there have been some reports of using colorimetric sensor arrays for the identification of sulfur-containing species [10,12,39]. For example, Yang et al. constructed a colorimetric sensor array by using Au-Ag nanocluster material [34], and Li et al. used ionically conductive MOFs as sensing materials to construct sensor arrays [10]. Meanwhile, a sensor array consisting of three kinds of Au NCs for the identification of different types of sulfur-containing species has been reported [12]. These previous studies indicated that the unique direct binding between sensor materials and analytes was the typical sensing strategy of colorimetric sensors for sulfur-containing compounds [15,27,39].

The use of nanozymes, one kind of nanomaterial with multiple enzyme-like activities and enzymatic catalytic properties, has become a novel strategy to design colorimetric sensors [26,36]. Compared with natural enzymes, nanozymes have the advantages of stability, economy and large-scale preparation and are widely applied in many fields, such as biosensing, biomedicine, antibacterial products and pollutant detection [13,29,5]. Among the numerous nanozyme materials, single-atom nanozymes (SANs) [11,21,23,8] are known for their high enzyme-like activities and unique structures of atomically dispersed metal sites. They have shown great potential to substitute natural enzymes in the domain of biochemical analysis, environmental control, disease treatment, and so on.

In this work, instead of using the classical sensing strategy, we fabricated atomic Co onto N-doped graphene (CoN_4-G) for the simultaneous detection of Na_2S, Na_2SO_3, $Na_2S_2O_3$ and $Na_2S_2O_8$. CoN_4-G exhibited excellent oxidase-like activity, and the catalysis mechanism was identified by density functional theory (DFT) calculations. Through LDA and colorimetric experiments, we found that the selectivity and sensitivity of the sensors were determined by different activities of nanozymes under different pH conditions and with different effects of distinct SCMs on TMBox. On CoN_4-G, TMB was directly oxidized by O_2 molecules without hydrogen peroxide (Scheme 1). Therefore, a sensor array (4 SCMs × 3 receptor units × 6 replicates) was successfully prepared. LDA produced a three-dimensional (3D) diagram with 100 % accuracy and no overlapping cross-validation, suggesting its success. To authenticate the differentiated capacity of the sensor array, distinct concentrations of unitary, binary, ternary and quaternary SCMs and interfering substances were analysed, showing that it possessed a wider detection range, lower detection limit, better stability and reproducibility, and stronger anti-interference. Accordingly, the sensor array may have broad prospects for application to food safety and environmental protection. In addition, we introduced the concept of automatic identification based on smartphones, thus breaking through the constraints of complex instruments and realizing on-site inspections.

2. Experimental section

2.1. Reagents and Instruments

Sodium sulfide (Na_2S), sulfite (Na_2SO_3), sodium thiosulfate ($Na_2S_2O_3$), sodium persulfate ($Na_2S_2O_8$), 3,3′,5,5′-tetramethylbenzidine (TMB), dimethyl sulfoxide (DMSO), acetic acid (HAc, 99.5 %), and sodium acetate (NaAc) were purchased from Shanghai Marcklin Biochemical Technology Co., Ltd. (Shanghai, China). Acetate buffer (HAc-NaAc) solutions (0.2 M) with different pH values were prepared by HAc and NaAc in distilled water. Cobalt nitrate hexahydrate ($Co(NO_3)_2{\cdot}6\,H_2O$), graphite powder (GO), nitric acid (HNO_3, 65 %), hydrochloric acid (HCl, 36 %), and sodium hydroxide (NaOH) were purchased from Xilong Chemical Industry (Guangdong, China). $NaNO_2$, ascorbic acid, uric acid, tartaric acid, cysteine and glucose were purchased from Shanghai Marcklin Biochemical Technology Co., Ltd. (Shanghai, China). NH_3 (99.99 %) and N_2 (99.99 %) were purchased from Juyang Gas (Changchun, China). Fresh eggs, red wine and milk were purchased from a local supermarket, and the soil was collected from the locality paper mill. A 96-well polystyrene plate was obtained from Jincanhua (Shenzhen, China). The other reagents were all of analytical grade and used without further purification.

Transmission electron microscopy (TEM) images were recorded using a Hitachi HT7700 transmission electron microscope (Tokyo, Japan) at 200 kV. X-ray diffraction (XRD) was recorded using copper filtered Kα radiation (λ = 1.5406 Å) on a RIGAKU D/MAX2550/PC diffractometer. Scanning electron microscopy (SEM) and high-angle annular dark-field scanning transmission electron microscopy (HAADF-STEM) images were recorded using a JEOS JSM 6700 F field-emission and aberration-corrected JEM-ARM 200 F microscope, respectively. Using Al Kα radiation on an ESCALAB 250 X-ray electron spectrometer, X-ray photoelectron spectroscopy (XPS) was performed. X-ray absorption spectra (XAS), including X-ray absorption near-edge structure (XANES) and extended X-ray absorption fine structure (EXAFS) spectra at the K-edge of Fe, were recorded at BL14W1 at the Shanghai Synchrotron Radiation Facility (SSRF), China. UV—Vis absorbance spectra were obtained from 200 to 800 nm wavelength at 0.5 nm interval setting using a Shimadzu UV-1900 spectrophotometer.

2.2. Preparation of CoN_4-G

Monatomic CoN_4-G nanomaterials were prepared by annealing a mixture of $CoCl_2$ and graphene oxide (GO) at high temperature (from 550° to 850°C) under a flowing ammonia atmosphere according to improved methods from previous research [11]. The CoN_4-G obtained by annealing at 750 °C was named CoN_4-G with a Co content of ca. 1.1 *wt*%.

2.3. Oxidase-like activity of CoN_4-G and kinetic assay

TMB, the most widely used natural oxidase substrate, was oxidized to bright blue oxidized TMB (TMB_{OX}) with a characteristic peak at 652 nm. Then, the catalytic activity of CoN_4-G was assessed by a chromogenic reaction from the oxidation of TMB. In brief, CoN_4-G (1 mg/mL) and TMB (2 mM) were dripped in acetate buffer (HAc buffer) with a pH of 3.0 at 25 °C for 30 min, and then the CoN_4-G was isolated by centrifugation at 10,000 rpm within 5 min. After that, the supernatant was moved into a quartz cuvette and analysed through a UV spectrophotometer at 652 nm. Efforts were then made to obtain the optimal incubation temperature, the right reaction time, the finest substrate concentration and buffer pH. The kinetics of CoN_4-G with TMB as the substrate were studied (25 °C, pH 3.0) by adding CoN_4-G (1 mg/mL) and different concentrations of TMB (0.2, 0.4, 0.6, 0.8, 1.0, 1.2, 1.4, 1.6, 1.8 and 2.0 mM). The initial absorption rate at 652 nm was recorded using a UV spectrophotometer. The Michaelis constant (K_m) and maximal reaction velocity (V_{max}) were calculated according to the Lineweaver—Burk plot. Then, the Michaelis—Menten equation was fitted for TMB at different concentrations (Eq. (1)).

$$\frac{1}{V} = \frac{1}{V_{\max}} + \frac{K_m}{V_{\max}} \times \frac{1}{[S]} \quad (1)$$

where V is the initial reaction velocity, V_{max} stands for the maximum reaction rate, $[S]$ is the concentration of the substrate, and K_m is the Michaelis—Menten constant. K_m is defined as the concentration of substrate at half the maximum catalytic rate, which reflects the affinity of CoN_4-G to the substrate.

2.4. DFT calculations

All first-principles DFT calculations concerning the OER theoretical mechanisms were performed using the Vienna Ab initio Simulation Package (VASP) based on the DFT plane-wave norm-conserving method. To calculate electronic structures and catalyse the reaction, the Perdew–Burke–Ernzerhof (PBE) functional was used to treat the electronic exchange–correlation interactions. Thus, first-principles quantum mechanics calculations were conducted, and the cut-off energy for the plane-wave basis set was set at 300 eV. The k-point sampling was a $2 \times 2 \times 1$ mesh by using the Monkhorst-Pack k-point grid. In the supercell configuration, a sufficiently large vacuum space of 15 Å was maintained along the z-axis. The Gibbs free energies of *OO, *OOH, *O and *OH on the surface of the modified electrode were evaluated by using DFT calculations. The Gibbs free energy changes of the reactions were calculated under standard conditions.

The crystal structures of the $(2 \times 2 \times 1)$ V_6O_{13} (0 0 1) surface obtained from the Materials Project online service (ID: mp-1201338), $(2 \times 2 \times 1)$ Fe_3O_4 (0 0 1) surface obtained from the Materials Project online service (ID: mp-19306), $(2 \times 2 \times 1)$ Au-Ag nanoparticle (1 1 0) surface obtained from the Materials Project online service (ID: mp-183214), and $(2 \times 2 \times 1)$ Cu nanocluster (1 1 1) surface obtained from the Materials Project online service (ID: mp-989782) were built to represent the different nanoenzyme catalytic surfaces, as shown in Fig. 3 and Figs. S5-S9.

2.5. Sensing procedure

The colorimetric detection for SCMs was built in the CoN_4-G-TMB reaction system. First, 10 μL CoN_4-G (1.0 mg/mL) was dripped in HAc buffer (pH 3.0, 4.0 and 4.5) containing 20 μL TMB (2 mM) and mixed together under optimal conditions (30 min, 25 ℃) before removing CoN_4-G. Subsequently, 5 μL of the target SCMs (Na_2S, Na_2SO_3, $Na_2S_2O_3$ and $Na_2S_2O_8$) with specific concentrations were dripped into the aforementioned solutions. After an additional 5 min incubation under the most suitable conditions, the absorbance at 652 nm was captured by the microplate reader, and the colorimetric signal was recorded. The data were normalized as ΔA (A_{blank} - A_{sample}) to eliminate the hidden bias caused by the variance in blank group data. Finally, the data matrix (4 SCMs × 3 receptor units × 6 replicates) was processed through LDA in Statistical Product and Service Solutions (SPSS 26.0).

In this study, the limit of detection (LOD) was calculated using the standard deviation method. Cubic standard deviation of blank absorbance (n = 10) was divided by the slope of the regression equation.

$$\mathrm{LOD} = (3 \times \delta)/\mathrm{k} \quad (2)$$

where δ is the standard deviation of the average blank signal and k is the slope of the linear calibration curve.

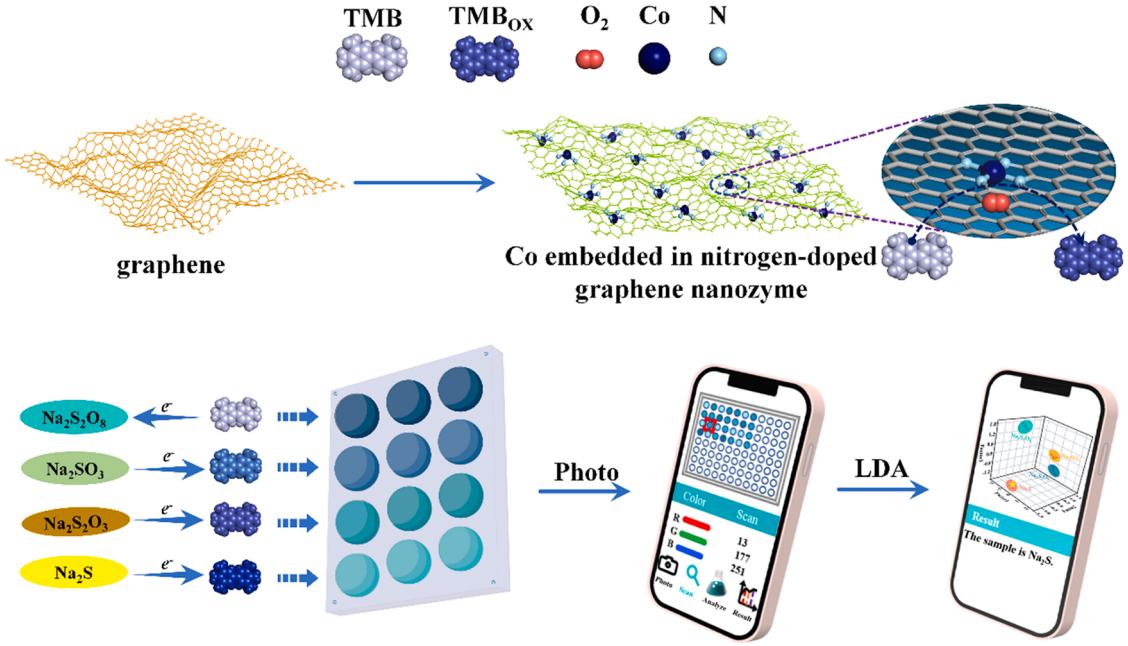

Scheme 1. Schematic diagram of a colorimetric intelligent detection platform for identifying Na_2S, Na_2SO_3, $Na_2S_2O_3$ and $Na_2S_2O_8$ based on the CoN_4-G nanozyme.

2.6. Detection of SCMs in real samples

The established array was used to detect SCMs in different real samples, including three environmental samples and three food samples. For accurate detection of targets in distinct systems, three environmental samples were collected: Sample 1 (collected from the soil 10 km away from the paper mill), Sample 2 (collected from the soil within 2 km outside the paper mill), and Sample 3 (collected from the soil inside the locality paper mill). The three food samples were Sample 4 (fresh milk), Sample 5 (wine after 2 years of storage at 25 °C), and Sample 6 (eggs after 1 week of storage at 25 °C).

Specifically, samples were pre-treated before the official start. After sieving out the stones and grass, the soil samples were crushed and dried for 30 min. One gram of each sample was weighed and dispersed into 5 mL of distilled water. After sonication for 10 min, the samples were centrifuged at 10,000 rpm for 5 min. The supernatant was collected and

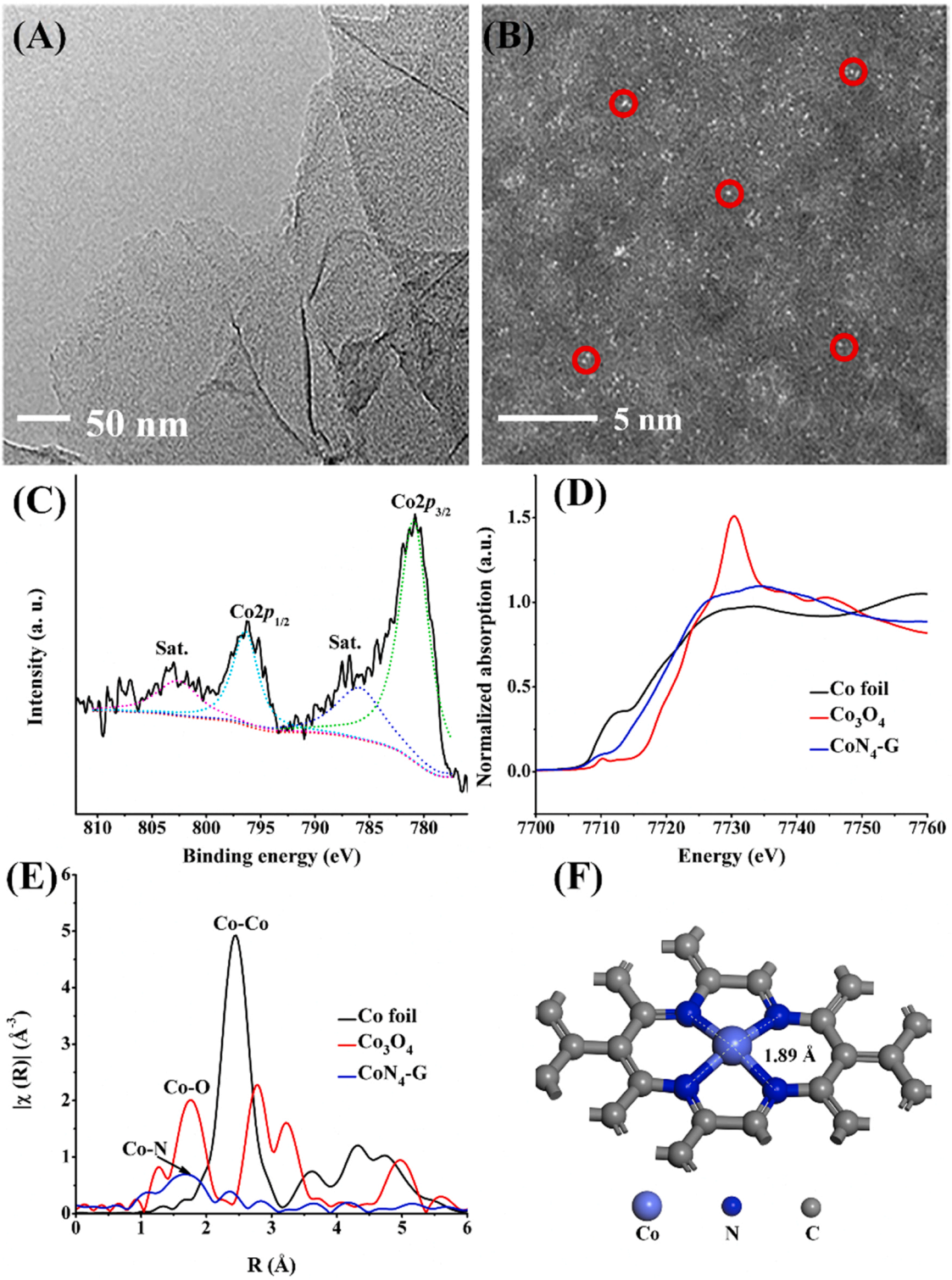

Fig. 1. (A) Representative TEM image of CoN_4-G. (B) HAADF-STEM image of CoN_4-G (C) High-resolution XPS Co 2*p* of CoN_4-G. (D) Normalized XANES spectra at Co K-edge of Co foil, Co_3O_4, CoN_4-G. (E) FT-EXAFS spectra of CoN_4-G at the Co K-edge (F) Atomic model of CoN_4-G cluster obtained from DFT calculation.

filtered to remove impurities. For the treatment of egg samples, the egg white was separated from the egg, homogenized with a homogenizer, and stored in a − 20 °C refrigerator. After the egg white sample returned to room temperature, a 1 g sample was added to 500 μL of water and centrifuged (5000 rpm, 5 min three times) to obtain the supernatant. Then, the supernatant was filtered three times with a filter membrane and diluted with HAc buffer at pH 3.0, 4.0, and 4.5. The signal was collected and analysed as mentioned above.

3. Results and discussion

3.1. Characterization of CoN_4-G

The morphology of CoN_4-G was characterized via TEM and STEM. As shown in Fig. 1 A, CoN_4-G had canonical morphologic features of graphene with a flake structure, and no CoO_x nanoparticles were seen in the entire detection area. Aberration-corrected microscopy confirmed the presence of atomically dispersed Co in CoN_4-G. In Fig. 1B, HAADF indicated that the Co element in the sample existed in an atomically dispersed form and that Co-based nanoparticles or clusters could no longer be found. In addition, no metal ion-based nanoparticles or clusters of the CoN_4-G sample were observed in the high-resolution STEM images, as shown in Fig. S1A. From the SEM image and the corresponding element maps (C, N, O and Co) obtained through EDX analysis (Fig. S1B), Co and N atoms were found to be uniformly dispersed on the nanosheets of the N-doped graphene. Interestingly, Co and N were always distributed adjacently, implying that there may be a bond between Co and N. The above results suggested that Co ions in CoN_4-G were in a mononuclear form, and the homogeneous dispersion of Co, N, C and O in CoN_4-G was also confirmed through elemental mapping on a much larger scale.

The oxidation state of Co ions in CoN_4-G was determined to be Co^{2+} according to the binding energies of Co $2p_{3/2}$ and Co $2p_{1/2}$ centred at 780.9 and 796.2 eV, respectively, as shown in Fig. 1 C [16]. Furthermore, XANES illustrated that the Co K-edge of XANES in the CoN_4-G sample was located between Co foil and Co_3O_4, indicating the same valence (Co^{2+}) in agreement with the XPS analysis (Fig. 1D). The EXAFS curve revealed the local structure of Co sites in CoN_4-G (Fig. 1E). Fig. 1E shows that the average Co environment within CoN_4-G was consistent with one O atom at a distance of 1.78 Å, four N atoms at a distance of 1.88 Å and two Co atoms at a distance of 2.45 Å. The O signal was caused by oxygen adsorption to the Co centre out of the plane with the graphene nanosheet structure. The signal from the four N atoms with a distance of 1.88 Å was evidence for the CoN_4-G configuration calculated by DFT, as shown in Fig. 1 F.

To further gain insight into the surface composition of CoN_4-G, XPS was performed, and the presence of C, N, O and Co peaks was found (Fig. S2A). As shown in Fig. S2B, the C 1 s peak could be deconvoluted into four peaks, corresponding to C═O (290.8), C-O (286.4 eV), C-N (285.5) and C═C (284.5 eV). In Fig. S2C, the N 1 s peak could be fitted into graphitic N (401.2 eV), pyrrolic N (400.2 eV), Co-N (399.3 eV) and pyridinic N (398.4 eV) [2,19].

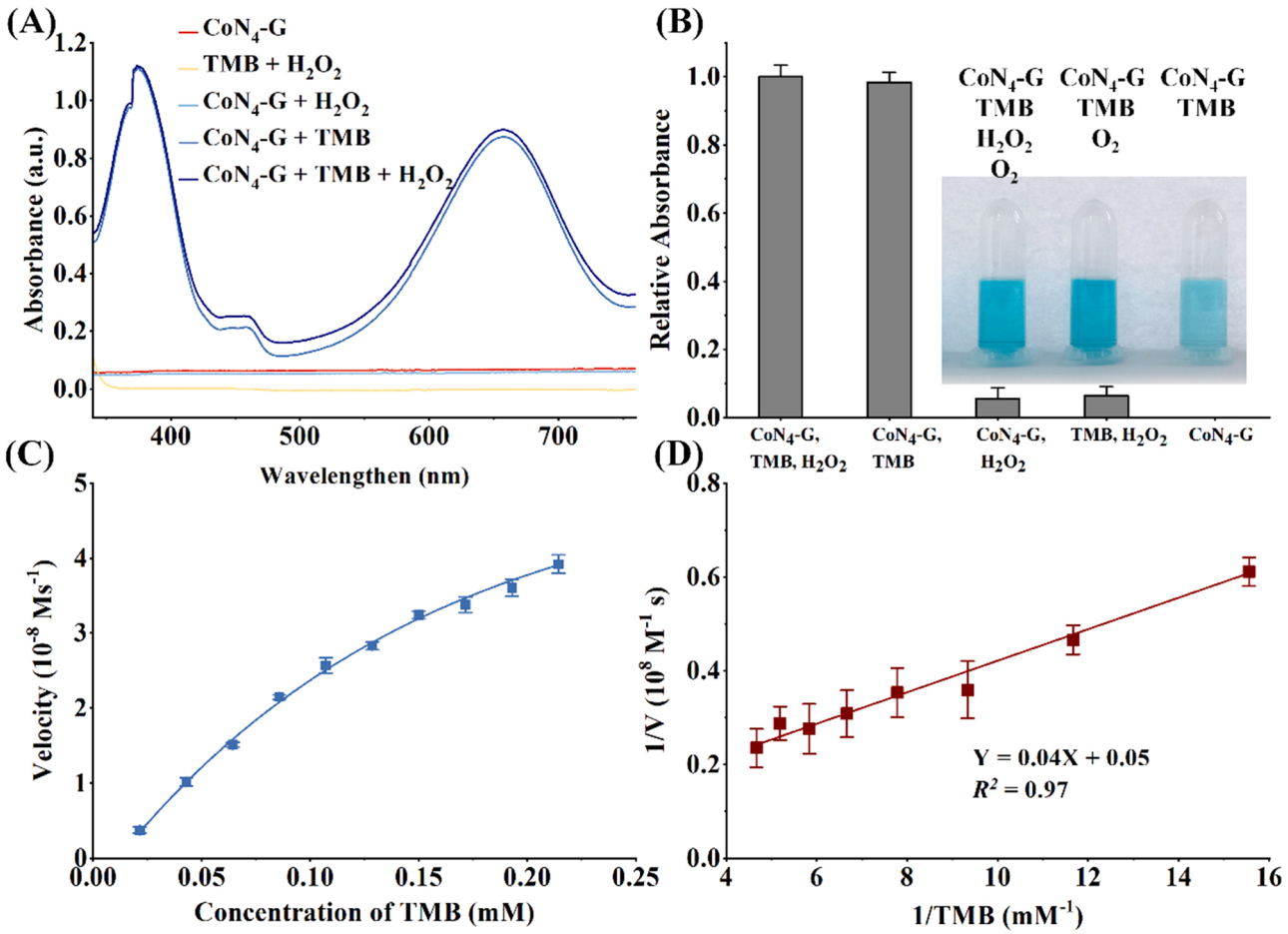

Fig. 2. Identification of the nano-enzyme activity of CoN_4-G. (A) UV–vis spectra of the different solutions and (B) The relative UV–vis absorptance of different systems (CoN_4-G + TMB + H_2O_2; CoN_4-G + TMB; CoN_4-G + H_2O_2; TMB + H_2O_2; CoN_4-G) at 652 nm. (inset: Photographs of TMB solutions in the absence and presence of H_2O_2 or O_2 oxidation reaction catalyzed by CoN_4-G.); (C) Michaelis−Menten curve of CoN_4-G with TMB and (D) Double-reciprocal plot activities of CoN_4-G with different concentrations of TMB.

3.2. CoN_4-G nanozymes mimicking oxidase activity

The enzyme-like activity of CoN_4-G was determined by employing TMB as the chromogenic substrate and compared to the peroxidase (POD) activity by dripping a certain concentration of hydrogen peroxide. UV—Vis spectra showed that TMB had no variation at 652 nm (Fig. 2A), and when mixed with H_2O_2. Fig. 2B illustrates the relative UV—vis absorptance of different systems (CoN_4-G + TMB + H_2O_2; CoN_4-G + TMB; CoN_4-G + H_2O_2; TMB + H_2O_2; CoN_4-G) at 652 nm. The results indicated that only the CoN_4-G + TMB + H_2O_2 and CoN_4-G + TMB groups had strong adsorption due to the presence of TMBox, implying that CoN_4-G could catalyse the oxidation of TMB with OXD-like activity in the absence of H_2O_2 and that the other components (CoN_4-G and TMB) had no obvious adsorption. In addition, it could be ruled out that CoN_4-G had POD-like activity because the addition of hydrogen peroxide did not cause a significant increase in absorbance (**inset in** Fig. 2B). To further study the effect of dissolved O_2 in the system on the oxidation and colour development of TMB, the oxygen was removed by blowing N_2 to create an oxygen-free environment. In Fig. 2B inset, the higher the O_2 concentration was in the degassing system, the deeper the blue colour of the system turned, indicating a higher degree of oxidation. Therefore, dissolved oxygen acted as an electron acceptor in the system and had a vital impact on the oxidation of TMB.

The V_{max} (16.03×10^{-8} M S^{-1}) and K_m (0.7738 mM) of CoN_4-G were obtained using the Michaelis—Menten model, and Fig. 2C, D shows the typical Michaelis—Menten curves and Lineweaver—Burk plots. According to the results of the Michaelis—Menten model (Fig. 2C, D and Table S1), CoN_4-G exhibited a higher V_m value than horseradish peroxidase (HRP) and other nanozymes, indicating that CoN_4-G had the potential to replace natural enzymes.

Furthermore, the optimal sensing ability of the array was obtained by optimizing limiting parameters such as system pH, incubation time and TMB concentration. First, the monatomic materials synthesized at different calcination temperatures were optimized. The results showed that the best catalytic performance of CoN_4-G was obtained when the calcination temperature was 750 ℃, as shown in Fig. S3A. Moreover, the pH value was considered the most critical parameter affecting the colour production of TMB oxidation catalysed by the nanozyme. Additionally, the acidic environment was conducive to the exertion of oxidase activity [32,37]. In the reaction system, pH values ranging from 3.0 to 6.5 had a significant effect on the oxidation of TMB in the absence of SCMs, as shown in Fig. S3B. When the pH was 3.5, the absorbance reached its highest point. Fig. S3C shows that the mixture time of CoN_4-G and TMB was also vital to the response signal. The absorbance values obviously increased over time within 30 min. Beyond this point, the absorbance remained relatively stable or even decreased slightly. Thus, 30 min was the optimal incubation time. Since TMB played a vital role in the colour rendering process of the system, the concentration must be optimized. Fig. S3D shows that the absorption spectrum increased continuously in the 2 mM range and very slowly in the range of 1.8–2 mM. Therefore, 2 mM was chosen as the optimal concentration in the follow-up work.

In this work, the detection capability of the sensor array could be determined by the oxidase-like catalytic activity of CoN_4-G. Therefore, the stability of the CoN_4-G nanozyme material was investigated first. As shown in Fig. S4A, within 1 month, the relative activity range of the CoN_4-G nanozyme was 97.7–100 %. With increasing storage time, the activity of the CoN_4-G nanozyme was basically unaffected. Subsequently, the reproducibility was also verified by detecting the relative absorption signals of five different batches of CoN_4-G nanozymes. As shown in Fig. S4B, when the TMB concentration was 1 mM, the relative standard deviation (RSD) of the 6 groups of CoN_4-G nanozyme materials was 1.53 %, suggesting that the reproducibility was good. Therefore, it could be proven that CoN_4-G nanozymes had potential reproducibility towards the needs of practical applications. Compared with the previous literature [31], the CoN_4-G nanozyme presented comparable stability and reproducibility, which could fully meet the requirements of practical detection.

3.3. Mechanism study of CoN_4-G nanozyme activity by DFT calculation

To further explore the catalytic activity of CoN_4-G, the oxidation process of the oxidase substrate on the monatomic CoN_4-G centre was calculated by DFT. Five catalyst modes of V_6O_{13}, Fe_3O_4, AuAg-Au nanoparticles, AuAg-Ag nanoparticles and Cu nanoclusters with different oxidase-like catalytic efficiencies were also constructed for comparison. In acidic medium, TMB was extremely easy to protonate. Therefore, H_2TMB^{2+} and TMB^{2+} were used as the unoxidized and oxidized oxidase substrates, respectively. In the reaction system, H_2TMB^{2+} could be oxidized to TMB^{2+} by surface O_2 molecules ($2\ H_2TMB^{2+} + O_2 \rightarrow 2TMB^{2+} + 2\ H_2O$ (g)) on the catalyst surface. The oxidation reaction was described in the following steps (1–5):

$$*+O_2 \rightarrow *OO \quad (1)$$

$$*OO + H_2TMB^{2+} \rightarrow *OOH + HTMB^{2+} \quad (2)$$

$$*OOH + HTMB^{2+} \rightarrow *O + H_2O + TMB^{2+} \quad (3)$$

$$*O + H_2TMB^{2+} \rightarrow *OH + HTMB^{2+} \quad (4)$$

$$*OH + HTMB^{2+} \rightarrow * + H_2O + TMB^{2+} \quad (5)$$

The Gibbs free energies of the reaction intermediates *OO, OOH* , O* and OH* on the catalyst surface were evaluated by DFT calculations. Fig. 3 illustrates the reaction route of six catalyst modes for the oxidation of TMB by surface O species. The corresponding structures of the intermediates in the five models of V_6O_{13}, Fe_3O_4, AuAg-Au, AuAg-Ag and Cu nanoclusters were optimized by DFT calculations, as shown in Figs. S5-S9.

In the first reaction step, the adsorption energy of Fe_3O_4 (0 0 1) for O_2 was the strongest (−2.39 eV), followed by V_6O_{13} (0 0 1), Cu (1 1 1) and CoN_4-G (−0.76 eV, −0.36 eV and −0.012 eV, respectively), while the adsorption barriers of AuAg-Au (1 1 0) and AuAg-Ag (1 1 0) to O_2 molecules were as high as 0.75 and 0.69 eV, respectively (Fig. 3B), suggesting that this reaction step became the rate-determining step. Then, the adsorbed O_2 could be easily reactivated and transferred to the surface OO species, which captured the H atom of H_2TMB^{2+} with low energies of − 2.59, − 0.92, − 0.42, − 0.35, − 0.65 and − 0.59 eV on V_6O_{13} (0 0 1), Cu (1 1 1), CoN_4-G, AuAg-Au (1 1 0) and AuAg-Ag (1 1 0), respectively, indicating that the intermediate OOH species was easily formed in the catalytic process. Subsequently, the surface OOH species captured the second H atom from $HTMB^{2+}$ to form surface O species with energies of − 0.80, − 1.90, − 0.96, − 1.03, and − 0.26 eV on V_6O_{13} (0 0 1), Cu (1 1 1), CoN_4-G, AuAg-Au (1 1 0) and AuAg-Ag (1 1 0), respectively. However, in the Fe_3O_4 (0 0 1) model, due to the absorption of the surface O species at the top of an Fe atom and the H_2O molecule floating on the surfaces of Fe_3O_4 (0 0 1), a high barrier of 1.50 eV was exhibited, implying that the H_2O molecule could hardly be removed and that this step was the rate-determining step. In the next reaction step, the H atom of H_2TMB^{2+} was easily adsorbed by the surface O species on the six catalytic models to form the surface OH species. In the last catalytic process, the surface OH species was transformed promptly into H_2O by capturing the H atom of the second $HTMB^{2+}$. The calculation showed that H_2O was released at high barriers of 1.37, 1.80 and 1.38 eV on Fe_3O_4 (0 0 1), V_6O_{13} (0 0 1) and Cu (1 1 1), respectively, suggesting that the final reaction was the rate-determining step for these models.

The calculation results demonstrated that V_6O_{13} (0 0 1), Fe_3O_4 (0 0 1), AuAg-Au (1 1 0), AuAg-Ag (1 1 0) and Cu (1 1 1) had high barriers of 0.93, 1.51, 0.69, 0.75 and 0.72 eV, respectively, which meant that these catalytic models could hardly accomplish the catalytic process (Fig. 3B). Due to the absence of the barrier in the whole reaction route, CoN_4-G had higher oxidase-like catalytic activity than the other catalytic models, in good agreement with the experimental results. Owing to the

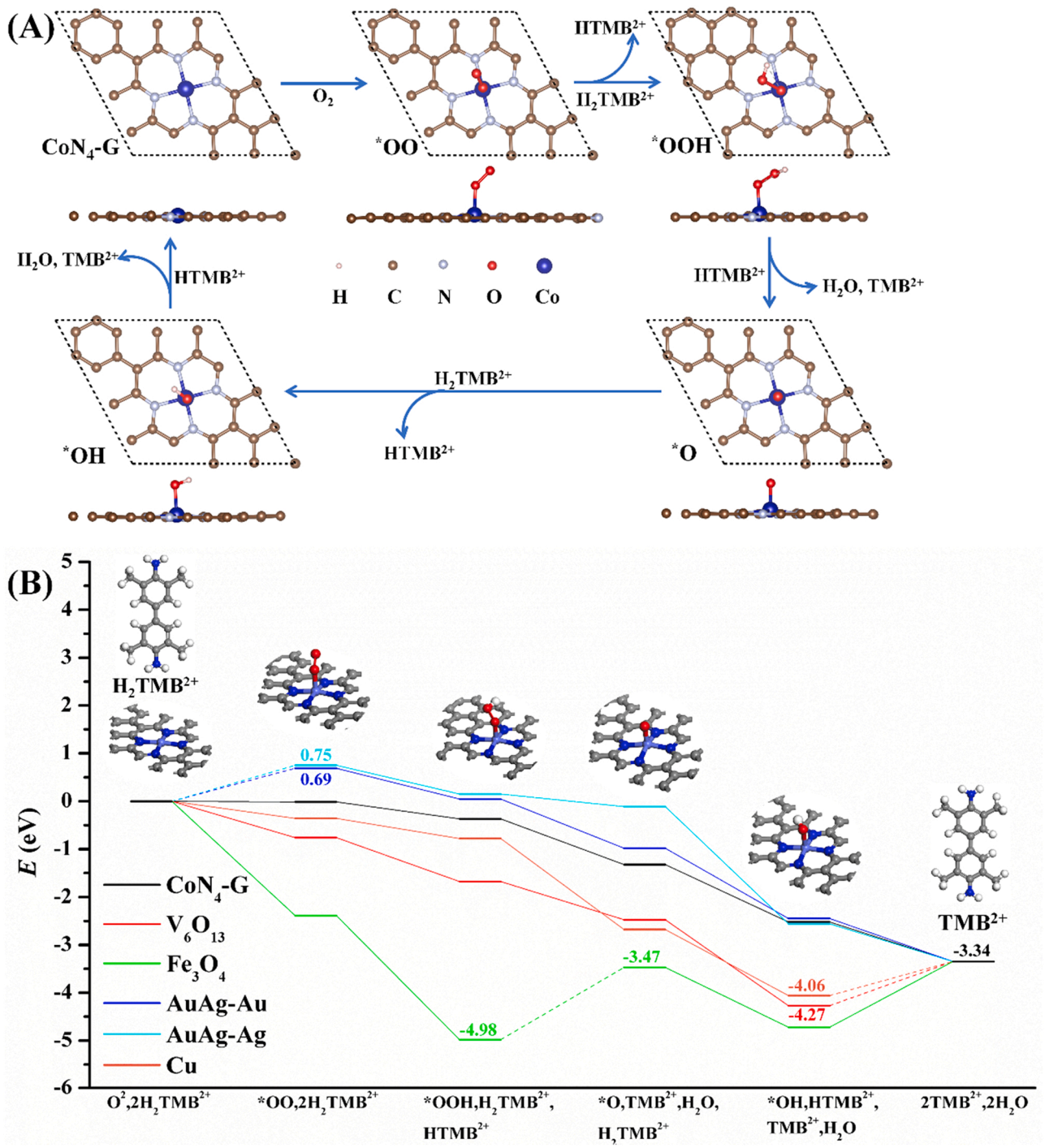

Fig. 3. DFT studies on the oxidase-like activity of six nanozyme catalytic models. (A) The reaction scheme of TMB oxidation and the intermediate structures of surface O species on the CoN_4-G (the top view and side view). (B) The free energy diagram of TMB oxidation reaction pathways on the surface of six catalytic models.

unique structure of monatomic cobalt embedded in nitrogen-doped graphene, O_2 molecules could be easily adsorbed on the surface of CoN_4-G, and the H_2O molecules transferred from OOH or OH could be dislodged from the surface quickly. Therefore, the high oxidase-like activity of CoN_4-G came from its monatomic structure.

3.4. Responses of colorimetric sensor array based on CoN_4-G to SCMs

Considering that different SCMs had obvious differences in the reduction activity to TMBox, a colorimetric sensor array was constructed. UV—Vis absorbance spectra of TMBox in the different reaction systems were recorded. To demonstrate the practical applications of this colorimetric sensor array, an LDA method was performed to identify four SCMs, namely, Na_2S, Na_2SO_3, $Na_2S_2O_3$ and $Na_2S_2O_8$. As shown in Fig. S10, the addition of SCMs significantly inhibited the absorbance of the CoN_4-G-TMB system, except for $Na_2S_2O_8$. For $Na_2S_2O_8$, the result was the opposite. The + 7 valence state strengthened the oxidation degree of TMB, which was then further oxidized by $Na_2S_2O_8$. Due to different sulfur valence states, SCMs had different reducing abilities to TMBox, which indicated that their different inhibitory effects on the oxidase-like activity of CoN_4-G provided the prerequisite for their identification.

Na_2S, Na_2SO_3, $Na_2S_2O_3$ and $Na_2S_2O_8$ were handpicked as targets. First, the colorimetric response range of the sensor array to the above SCMs was investigated, initially set as 10, 20, 40, 60, 80 and 100 μM. If SCMs existed in the detection system, SCMs could reduce TMBox based on their own reducibility rather than directly interfering with the oxidation of TMB. The reduction degree of TMBox depended on the S atom valence state of the SCMs. The lower the S atom valence state, the stronger the reducibility capability of SCMs. Therefore, the reducibility capability of the four SCMs decreased in the following sequence: Na_2S (−2) > $Na_2S_2O_3$ (+2) > Na_2SO_3 (+4) > $Na_2S_2O_8$ (+7). When different SCMs appeared in the system, they were accompanied by different colorimetric signals, intuitively indicating that each target SCM had a one-to-one correspondence with its unique fingerprint spectrum. A more precise analysis of the optical fingerprint spectra was performed with

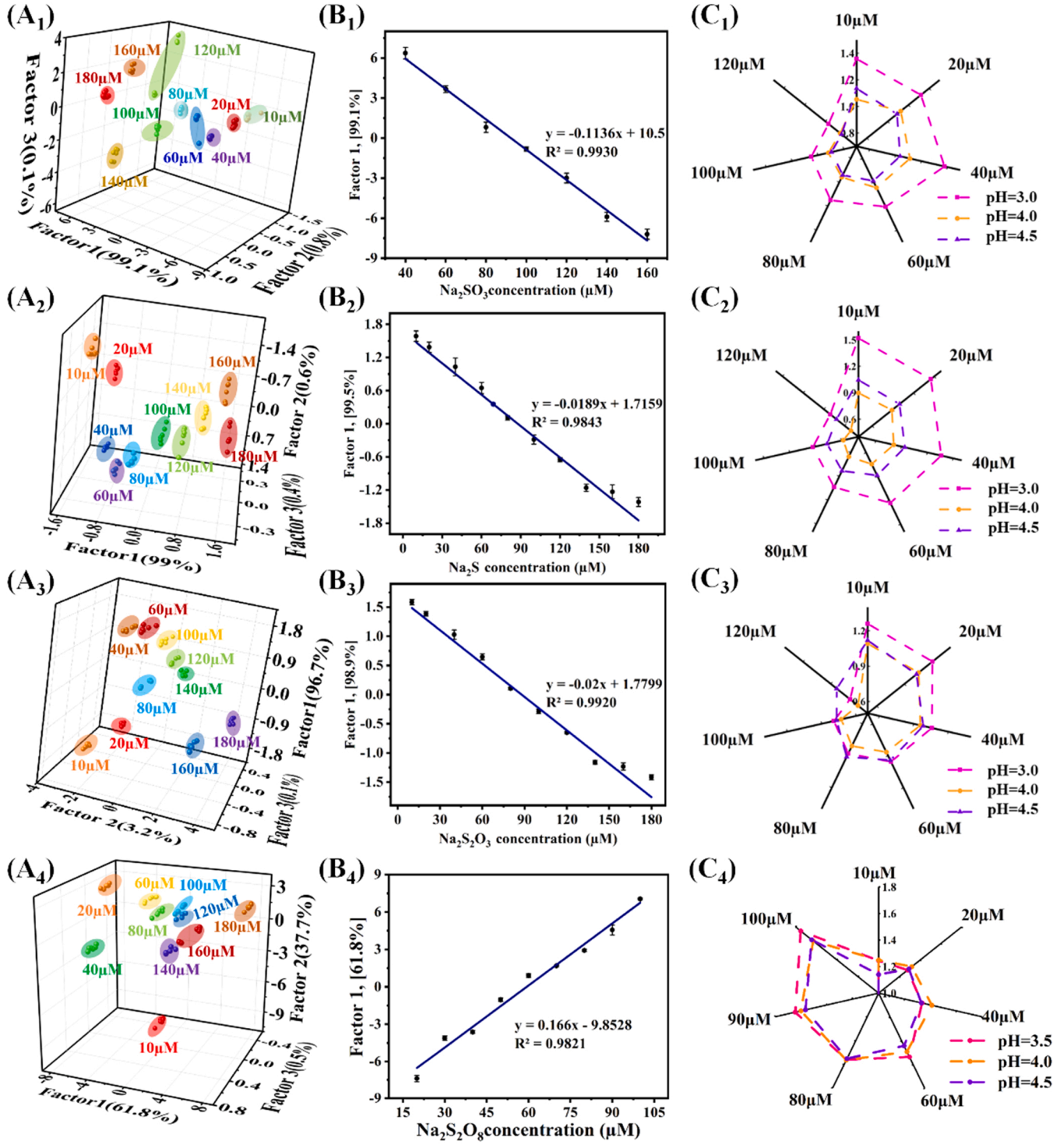

Fig. 4. LDA score plots for the colorimetric response of the sensor array with different concentrations of sulfur-containing compounds (A_1: Na_2SO_3, A_2: Na_2S, A_3: $Na_2S_2O_3$, A_4: $Na_2S_2O_8$). (B_1-B_4) Plots of the discriminant factor 1 versus the concentrations of sulfur-containing compounds. Response charts of the three recognition elements (pH = 3.0, pH = 4.0, and pH = 4.5) to different concentrations of a given sulfur-containing compounds (C_1: Na_2SO_3, C_2: Na_2S, C_3: $Na_2S_2O_3$, C_4: $Na_2S_2O_8$). The y-axis scale represented the absorbance value (unit: a.u.) of TMBox in the reaction system.

the aid of LDA. In Fig. S11, the output data (4 SCMs ×3 receptor units ×6 replicates) from LDA of Na_2S, Na_2SO_3, $Na_2S_2O_3$ and $Na_2S_2O_8$ were plotted according to their first three discriminant factors accounting for approximately 100 % of the variance. It was observed that each sulfur-containing compound formed tight clusters that were not only clearly separated from each other but also did not overlap, marking the success of our constructed sensing array in discriminating various SCMs at the same concentration. In the next step, the constructed sensing arrays

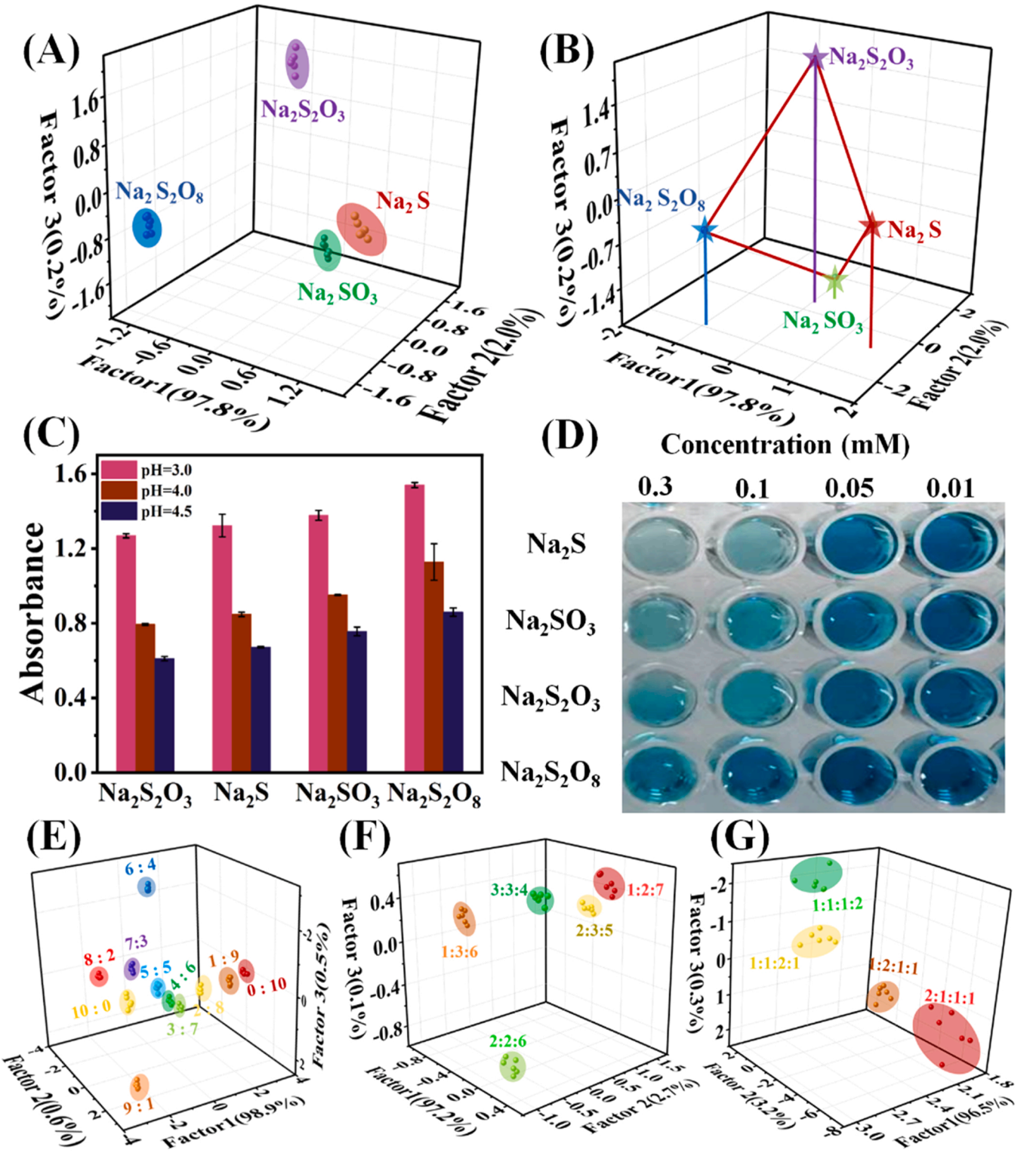

Fig. 5. (A) Canonical score plot, (B) centroid diagram, (C) colorimetric responses, and (D) color difference map of four sulfur-containing compounds (all at 5 μM) on the sensor array (The concentrations of $Na_2S_2O_8$ are 0.01, 0.05, 0.1 and 0.3 mM from left to right). Canonical score plots of (E) binary sulfur-containing compounds mixtures ($Na_2S_2O_8$/Na_2S = 0:10, 1:9, 2:8, 3:7, 4:6, 5:5, 6:4, 7:3, 8:2, 9:1 and 10:0), (F) ternary sulfur-containing compounds mixtures (Na_2S /$Na_2S_2O_8$ /Na_2SO_3 = 1:2:7, 1:3:6, 2:2:6, 2:3:5 and 3:3:4) and (G) quaternary sulfur-containing compounds mixtures ($Na_2S_2O_3$ /Na_2S /Na_2SO_3 /$Na_2S_2O_8$ = 2:1:1:1, 1:2:1:1, 1:1:2:1 and 1:1:1:2) at different molar ratios.

were verified to be able to distinguish different concentrations belonging to the same SCMs. Ten concentrations of Na_2S, Na_2SO_3, $Na_2S_2O_3$ and $Na_2S_2O_8$ were selected, including 10, 20, 40, 60, 80, 100, 120, 140, 160 and 180 μM. Based on the LDA data, Fig. 4 corresponding to the four SCMs in turn was drawn in the 3D standard score plot. In each graph, the 60 data points obtained (10 concentrations × 6 replicates) clearly yielded 10 clusters corresponding to each target SCM. From the 3D standard score plots, different concentrations of a given sulfur-containing compound could be distinguished, indicating that the colorimetric sensor array could effectively discriminate diverse SCMs at ten concentrations by the LDA technique. Since each sulfur-containing compound had its own specific position, the value of the three pH conditions for the specific SCMs could be located with only knowledge of the absorbance values of the pH for these SCMs, revealing the specific response between pH and SCMs. In the experiment, we found that this hypothesis could be realized when the number of experiments was large enough.

To investigate the sensitivity of the constructed sensing array, the quantitative detection performance for individual SCMS was identified. As seen in Fig. 4 A_1-A_4, Na_2S, Na_2SO_3, $Na_2S_2O_3$ and $Na_2S_2O_8$ within the concentration range of 10–180 μM were well differentiated in the 3D LDA plot. To confirm that the sensing array was competent to discriminate lower concentrations of SCMs, a 5 μM target of SCMs was used in the experiment. In Fig. 5A-D, the changes in absorbance and colour caused by different SCMs were significantly different, indicating that the colorimetric sensor array could also achieve the goal of discrimination at lower concentrations.

Higher requirements on the sensing array were put forward after the confirmation that it was capable of distinguishing different concentrations of SCMs, and it succeeded in distinguishing mixtures of binary, ternary and quaternary SCMs at different molar ratios ($Na_2S_2O_8/Na_2S$ = 0:10, 1:9, 2:8, 3:7, 4:6, 5:5, 6:4, 7:3, 8:2, 9:1 and 10:0; Na_2S /$Na_2S_2O_8$ /Na_2SO_3 = 1:2:7, 1:3:6, 2:2:6, 2:3:5 and 3:3:4; $Na_2S_2O_3$ /Na_2S /Na_2SO_3 /$Na_2S_2O_8$ = 2:1:1:1, 1:2:1:1, 1:1:2:1 and 1:1:1:2) with a total concentration of 5 μM. In Fig. 5E-G, these SCM mixtures were obviously separated from each other in 3D LDA plots. The results showed that the constructed sensing array was still sensitive in the discrimination of sulfur-containing compound mixtures, which signified its great application potential for the identification of complex components.

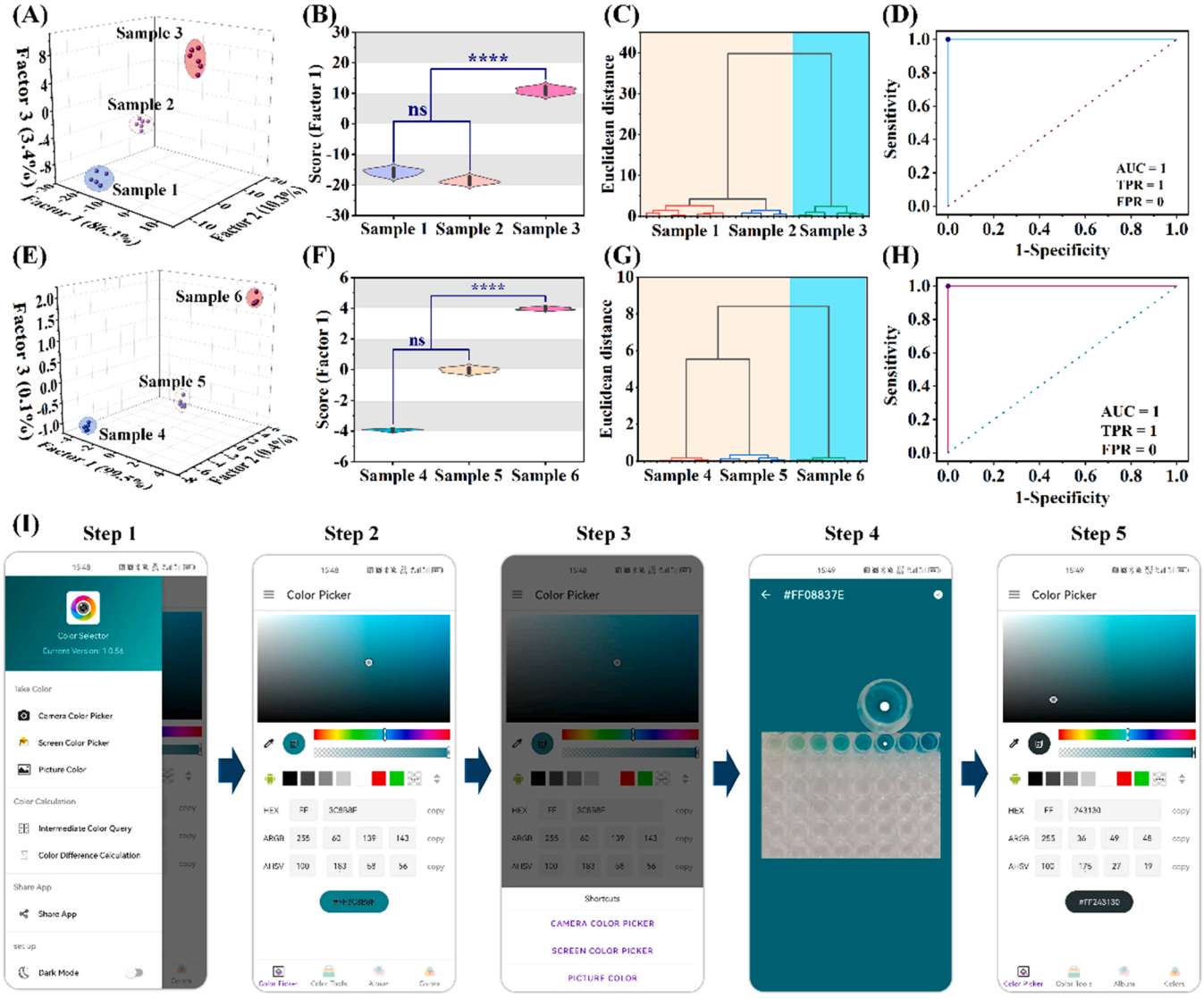

Fig. 6. 3D canonical score plots of the sensor array toward three environmental samples (A) and three food samples (E) with different SCMs concentration. Plot of the factor 1 and HCA dendrogram vs three environmental samples (B and C) and three food samples (F and G), respectively. ROC curve of the sensor array in the SCMs assessment of environmental samples (D) and food samples (H). (I) Smartphone platform based on "Color Selector" APP software for detecting SCMs.

3.5. Selectivity of the colorimetric sensor array

To confirm the anti-interference ability of the sensing assay for the simultaneous determination of Na_2S, Na_2SO_3, $Na_2S_2O_3$ and $Na_2S_2O_8$ in complicated solution systems, the resistance of the sensing array to various interfering substances, including NO_2^-, ascorbic acid, uric acid, tartaric acid, cysteine and glucose, at a concentration of 5 μM was tested. Although various interfering substances also produced response signals, they were significantly different from the responses elicited by the target substances, indicating that the presence of interfering substances did not affect the identification of SCMs. In the LDA score plot (Fig. S12), the relevant SCMs and interfering substances were obviously separated from each other without any crossover. The results showed that the sensor array had good specificity for the four SCMs (Na_2S, Na_2SO_3, $Na_2S_2O_3$ and $Na_2S_2O_8$).

3.6. Discrimination of SCMs in real samples

Various types of actual samples were differentiated using LDA and hierarchical cluster analysis (HCA) to evaluate the practical feasibility of the colorimetric sensor array based on different SCM contents (Fig. 6). Due to the use of bleach, SO_3^{2-} and $S_2O_3^{2-}$ became the main pollution of the paper mill. Fig. 6 A shows that the three types of environmental samples from the paper mill were precisely classified. Due to the significant difference in SCM content, the clusters of Sample 1 and Sample 2 with low concentrations of SCMs were located at the bottom area and were far from the cluster of Sample 3 at the top region in the 3D canonical score plot. Colorimetric response patterns $[(A\text{-}A_0)/A_0]$ and the heatmap of three samples based on the sensor array also had excellent identification (Fig. S13). Moreover, an obvious difference was presented in the violin chart score of discriminant Factor 1 vs. samples (Fig. 6B). HCA further showed that the three samples could be accurately classified according to SCM concentration. Sample 1 and Sample 2 were further assigned to the same cluster due to the similar SCM concentrations compared with Sample 3 (Fig. 6 C). The receiver operating characteristic (ROC) curve was used to further evaluate the performance of LDA for the identification of SCMs. Fig. 6D illustrates that the area under the curve (AUC), true positive rate (TPR) and false-positive rate (FPR) of this environmental sample classification model were 1, 1 and 0, respectively, implying that this sensor array could be applied in the SCM assessment of environmental samples with high accuracy.

In addition, there was a similar effect in the food samples. Eggs could produce S^{2-}, and the content of S^{2-} increased with increasing storage time. Due to the addition of SO_2, wine also contained a certain amount of SO_3^{2-}. Then, the difference in SCM content was analysed by LDA to ensure the classification of the three food samples (Fig. 6E and Fig. S14). The violin chart score of discriminant Factor 1 vs. samples showed that the difference in three samples with different SCM contents was remarkable (Fig. 6 F). Fig. 6 G illustrates that Sample 4 and Sample 5 could be assigned to the same cluster as Sample 6. Furthermore, the high accuracy of this sensor array for food sample detection was also confirmed by the ROC curve (Fig. 6H). The above test strategy has been widely used in colorimetric sensor array fields [38,40]. For example, Yang et al. constructed a colorimetric sensor array based on AuAgNCs for the discrimination of sulfur bacteria [34], and a nanozyme sensor array based on aptamer-modified C_3N_4 nanosheets realized the accurate identification of cancer [14]. Therefore, we believe that the colorimetric sensor array designed in this work could be a promising candidate for the environmental detection of SCMs.

At present, there are some studies on colorimetric sensor arrays based on nanozyme materials. Zhu et al. reported heteroatom-doped graphene materials with peroxidase-mimicking activity and fabricated colorimetric sensor arrays [41]. In the presence of H_2O_2, the discrimination of different pesticides was realized by the colorimetric sensor array. Meanwhile, an oxidase mimic material based on MOFs was also reported, and the constructed sensor array could be used for quantifying and discriminating multiple antioxidants by H_2O_2 [17]. Wang et al. achieved the identification of nanozyme sensor arrays and a biological mercaptan based on peroxide-like Pt, Ru, and Ir nanoenzymes [28]. However, the structures and reaction mechanisms of nanozyme materials are still unclarified. In this work, we prepared 2D monatomic Co embedded in a nitrogen-doped graphene nanozyme (CoN_4-G) with atomic Co as the active centre. Due to this unique structure, CoN_4-G exhibited excellent oxidase-mimicking activity and could directly catalyse the oxidization of TMB without depending on H_2O_2. Because of the high oxidase-mimicking activity of this novel monatomic Co nanozyme material, the sensing performance of this sensor array could achieve or surpass those of the previous literature (Tables S1 and S2).

To meet the practical application of CoN_4-G-based sensors for SCM detection, the idea of building a convenient smartphone platform based on "Color Selector" APP software that integrated colorimetric signals was proposed. As shown in Fig. 6I, the following five steps were completed with the assistance of a smartphone from step 1 to step 5, and the detailed operation process is shown in the Supporting Information. Ultimately, we hoped to successfully build this smartphone-based intuitive and convenient method for on-site detection of SCM species and their concentrations without the need for expensive equipment.

4. Conclusions

In this work, we have successfully synthesized monatomic Co embedded in N-doped graphene nanozymes. Based on the unique structure, CoN_4-G exhibited much higher oxidase-like catalytic performance (V_{max} of 16.03×10^{-8} M S^{-1}) than native enzymes. SCM antioxidants could inhibit the response of the CoN_4-G-TMB system with remarkable colour fading. The molecular mechanism was explored by DFT calculations. According to this molecular mechanism, a simple and effective visual colorimetric sensor array was established. The core was that the oxidase-like activity of monatomic CoN_4-G nanozymes could catalyse the colour development of TMB in the system without H_2O_2, and the enzyme activity was greatly regulated by pH. When the target was dripped in, a specific fingerprint could be generated to realize the identification and quantitative analysis of various SCMs. LDA analysis showed that the array could not only recognize four kinds of SCMs at the concentrations as low as 5 μM, differentiate mixtures of SCMs with various molar ratios, and identify individual SCMs at various concentrations but also have outstanding resistance to interference. Most worth mentioning is the recognition of SCMs in perplexed systems such as water, milk, red wine, and egg white, marking the great future of the sensing strategy in food safety, environmental protection and disease diagnosis. Finally, we creatively proposed to develop a smartphone-based autonomous detection app, which is expected to promote the on-site detection of SCMs with colorimetric sensing arrays in the future.

Environmental implication

In this work, we constructed a ternary channel colorimetric sensor array to detect multiple SCMs simultaneously in real samples. This colorimetric sensing array is expected to be used for environmental monitoring applications and the reduction of environment-related health risks.

CRediT authorship contribution statement

Fengling Wu: Investigation, Methodology, Data curation. **Hongsu Wang:** Conceptualization, Writing – review & editing, Supervision. **Lifang Wu:** Methodology, Data curation. **Jingqi Guan**: Formal analysis, Writing – original draft. **Xiaodi Niu:** Project administration, Funding acquisition, Supervision, Writing – review & editing.

Declaration of Competing Interest

The authors declare that they have no known competing financial interests or personal relationships that could have appeared to influence the work reported in this paper.

Data availability

No data was used for the research described in the article.

Acknowledgements

This work was supported by the National Natural Science Foundation of China (No. 32072919 and 22075099), Jilin Scientific and Technological Development Program (No. 20200402060NC and 20230508031RC), the Natural Science Foundation of Jilin Province (No. 20220101051JC), and the Education Department of Jilin Province (No. JJKH20220967KJ).

Appendix A. Supporting information

Supplementary data associated with this article can be found in the online version at doi:10.1016/j.jhazmat.2023.131643.

References

[1] Abdussalam, A., Yuan, F., Ma, X.G., Du, F.X., Zholudov, Y.T., Zafar, M.N., et al., 2020. Tris(2,2 '-bipyridine)ruthenium(II) electrochemiluminescence using rongalite as coreactant and its application in detection of foodstuff adulteration. J Electroanal Chem 857, 113752. https://doi.org/10.1016/j.jelechem.2019.113752.

[2] Atchudan, R., Perumal, S., Karthikeyan, D., Pandurangan, A., Lee, Y.R., 2015. Synthesis and characterization of graphitic mesoporous carbon using metal–metal oxide by chemical vapor deposition method. Microporous Mesoporous Mater 215, 123–132. https://doi.org/10.1016/j.micromeso.2015.05.032.

[3] Balasurya, S., Syed, A., Thomas, A.M., Marraiki, N., Elgorban, A.M., Raju, L.L., et al., 2021. Development of silver-polyvinylpyrrolidone nanocomposite for the selective and sensitive detection of sulfide from aqueous sample and its antimicrobial activity. Mater Chem Phys 257, 123789. https://doi.org/10.1016/j.matchemphys.2020.123789.

[4] Bordbar, M.M., Tashkhourian, J., Hemmateenejad, B., 2022. Paper-based optical nose made with bimetallic nanoparticles for monitoring ignitable liquids in gasoline. ACS Appl Mater Interfaces 14 (6), 8333–8342. https://doi.org/10.1021/acsami.1c24194.

[5] Cai, Y.Y., Liu, C.Y., Wang, J., Liu, X., Zhang, Y.J., Yang, S.Q., et al., 2021. Cu_xO nanorods with excellent regenerable NADH peroxidase mimics and its application for selective and sensitive fluorimetric ethanol sensing. Anal Chim Acta 1186, 339126. https://doi.org/10.1016/j.aca.2021.339126.

[6] Chu, J., Guo, W.T., 2018. Electrochemical sensor for sulfide determinationin food additives. Funct Mater 25 (1), 184–187. https://doi.org/10.15407/fm25.01.184.

[7] Han, X., Liu, L., Gong, H., Luo, L., Han, Y., Fan, J., et al., 2022. Dextran-stabilized Fe-Mn bimetallic oxidase-like nanozyme for total antioxidant capacity assay of fruit and vegetable food. Food Chem 371, 131115. https://doi.org/10.1016/j.foodchem.2021.131115.

[8] Jiang, D., Liu, Q., Wang, K., Qian, J., Dong, X.Y., Yang, Z.T., et al., 2014. Enhanced non-enzymatic glucose sensing based on copper nanoparticles decorated nitrogen-doped graphene. Biosens Bioelectron 54, 273–278. https://doi.org/10.1016/j.bios.2013.11.005.

[9] Jiang, L.R., Chen, T.H., Song, E.W., Fan, Y., Min, D.Y., Zeng, L.T., et al., 2022. High-performance near-infrared fluorescence probe for fast and specific visualization of harmful sulfite in food, living cells, and zebrafish. Chem Eng J 427, 113563. https://doi.org/10.1016/j.cej.2021.131563.

[10] Li, L., Zhang, S., Lu, Y., Zhang, J., Zhang, X., Wang, R., et al., 2021. Highly selective and sensitive detection of volatile sulfur compounds by ionically conductive metal-organic frameworks. Adv Mater 33 (52), e2104120. https://doi.org/10.1002/adma.202104120.

[11] Li, M., Wu, S.J., Yang, X.Y., Hu, J., Peng, L., Bai, L., et al., 2017. Highly efficient single atom cobalt catalyst for selective oxidation of alcohols. Appl Catal a Gen 543, 61–66. https://doi.org/10.1016/j.apcata.2017.06.018.

[12] Li, W.T., Sun, X.M., Zhao, X., Wang, W., Xu, S.H., Luo, X.L., 2020. Rapid pattern recognition of different types of sulphur-containing species as well as serum and bacteria discrimination using Au NCs-Cu^{2+} complexes. Chin Chem Lett 31 (9), 2473–2477. https://doi.org/10.1016/j.cclet.2020.04.027.

[13] Liu, M., Mou, J.S., Xu, X.H., Zhang, F.F., Xia, J.F., Wang, Z.H., 2020. High-efficiency artificial enzyme cascade bio-platform based on MOF-derived bimetal nanocomposite for biosensing. Talanta 220, 121374. https://doi.org/10.1016/j.talanta.2020.121374.

[14] Liu, M.X., Zhang, H., Zhang, X.W., Chen, S., Yu, Y.L., Wang, J.H., 2021. Nanozyme sensor array plus solvent-mediated signal amplification strategy for ultrasensitive ratiometric fluorescence detection of exosomal proteins and cancer identification. Anal Chem 93 (25), 9002–9010. https://doi.org/10.1021/acs.analchem.1c02010.

[15] Liu, Y., Zhang, J., Zhao, X., Li, W., Wang, J., Gao, Y., et al., 2020. Water-soluble carbon dots with blue, yellow and red emissions: mechanism investigation and array-based fast sensing application. Chem Commun 56 (29), 4074–4077. https://doi.org/10.1039/d0cc01156h.

[16] Long, J., Xie, X., Xu, J., Gu, Q., Chen, L., Wang, X., 2012. Nitrogen-doped graphene nanosheets as metal-free catalysts for aerobic selective oxidation of benzylic alcohols. ACS Catal 2 (4), 622–631. https://doi.org/10.1021/cs3000396.

[17] Lu, Y., Zhang, X., Huang, Y., 2022. Tuning nanozyme property of Co@NC via V doping to construct colorimetric sensor array for quantifying and discriminating antioxidant phenolic compounds. Biosens Bioelectron 215, 114567. https://doi.org/10.1016/j.bios.2022.114567.

[18] Lu, Z., Lu, N., Xiao, Y., Zhang, Y., Tang, Z., Zhang, M., 2022. Metal-nanoparticle-supported nanozyme-based colorimetric sensor array for precise identification of proteins and oral bacteria. ACS Appl Mater Interfaces 14 (9), 11156–11166. https://doi.org/10.1021/acsami.1c25036.

[19] Ma, C.Y., Mu, Z., Li, J.J., Jin, Y.G., Cheng, J., Lu, G.Q., et al., 2010. Mesoporous Co_3O_4 and Au/Co_3O_4 catalysts for low-temperature oxidation of trace ethylene. J Am Chem Soc 132 (8), 2608–2613. https://doi.org/10.1021/ja906274t.

[20] Moreira, B.M., Lima, A.P., Munoz, R.A.A., Petruci, J.F.D., 2021. An indirect electrochemical method for aqueous sulfide determination in freshwaters using a palladium chelate as a selective sensor. Talanta 231, 122413. https://doi.org/10.1016/j.talanta.2021.122413.

[21] Niu, X.H., Shi, Q.R., Zhu, W.L., Liu, D., Tian, H.Y., Fu, S.F., et al., 2019. Unprecedented peroxidase-mimicking activity of single-atom nanozyme with atomically dispersed Fe-N-x moieties hosted by MOF derived porous carbon. Biosens Bioelectron 142, 111495. https://doi.org/10.1016/j.bios.2019.111495.

[22] Qin, W.J., Su, L., Yang, C., Ma, Y.H., Zhang, H.J., Chen, X.G., 2014. Colorimetric detection of sulfite in foods by a TMB-O-$_2$-C_{o3O4} nanoparticles detection system. J Agr Food Chem 62 (25), 5827–5834. https://doi.org/10.1021/jf500950p.

[23] Sa, Y.J., Park, S.O., Jung, G.Y., Shin, T.J., Jeong, H.Y., Kwak, S.K., et al., 2019. Heterogeneous Co-N/C electrocatalysts with controlled cobalt site densities for the hydrogen evolution reaction: structure-activity correlations and kinetic insights. ACS Catal 9 (1), 83–97. https://doi.org/10.1021/acscatal.8b03446.

[24] Song, N., Zhong, M.X., Xu, J.Q., Wang, C., Lu, X.F. 2022. Single-atom iron confined within polypyrrole-derived carbon nanotubes with exceptional peroxidase-like activity for total antioxidant capacity. Sens Actuators B Chem. 351, p. 130969. Available from: https://doi.org/10.1016/j.snb.2021.130969.

[25] Turan, I.S., Sozmen, F., 2014. A chromogenic dioxetane chemosensor for hydrogen sulfide and pH dependent off-on chemiluminescence property. Sens Actuators B Chem 201, 13–18. https://doi.org/10.1016/j.snb.2014.04.101.

[26] Wang, M., Chang, M., Chen, Q., Wang, D., Li, C., Hou, Z., et al., 2020. Au_2Pt-PEG-Ce_6 nanoformulation with dual nanozyme activities for synergistic chemodynamic therapy / phototherapy. Biomaterials 252, 120093. https://doi.org/10.1016/j.biomaterials.2020.120093.

[27] Wang, S., Ren, J.S., Shan, L.Y., Sun, X.Y., Di, B., Gu, N., et al., 2020. Triplexed tracking labile sulfur-containing species on a single-molecule "Nezha" sensor. Anal Chem 92 (3), 2672–2679. https://doi.org/10.1021/acs.analchem.9b04688.

[28] Wang, X., Qin, L., Zhou, M., Lou, Z., Wei, H., 2018. Nanozyme sensor arrays for detecting versatile analytes from small molecules to proteins and cells. Anal Chem 90 (19), 11696–11702. https://doi.org/10.1021/acs.analchem.8b03374.

[29] Wu, J.H., Lv, W.X., Yang, Q.T., Li, H.Y., Li, F., 2021. Label-free homogeneous electrochemical detection of MicroRNA based on target-induced anti-shielding against the catalytic activity of two-dimension nanozyme. Biosens Bioelectron 171, 112707. https://doi.org/10.1016/j.bios.2020.112707.

[30] Wu, M.X., Chen, H.Y., Fan, Y., Wang, S.T., Hu, Y., Liu, J., et al., 2022. Carbonyl flavor compound-targeted colorimetric sensor array based on silver nitrate and o-phenylenediamine derivatives for the discrimination of Chinese Baijiu. Food Chem 372, 131216. https://doi.org/10.1016/j.foodchem.2021.131216.

[31] Xing, Z., Zhang, S., Wang, H., Ma, H., Wu, D., Fan, D., et al., 2022. Addressable label-free photoelectric sensor array with self-calibration for detection of neuron specific enolase. Anal Chem 94 (19), 6996–7003. https://doi.org/10.1021/acs.analchem.1c05577.

[32] Xu, C., Lin, Y., Wang, J., Wu, L., Wei, W., Ren, J., et al., 2013. Nanoceria-triggered synergetic drug release based on CeO(2) -capped mesoporous silica host-guest interactions and switchable enzymatic activity and cellular effects of CeO(2). Adv Healthc Mater 2 (12), 1591–1599. https://doi.org/10.1002/adhm.201200464.

[33] Yan, Y.H., Zhang, K., Yu, H., Zhu, H.J., Sun, M.T., Hayat, T., et al., 2017. Sensitive detection of sulfide based on the self-assembly of fluorescent silver nanoclusters on the surface of silica nanospheres. Talanta 174, 387–393. https://doi.org/10.1016/j.talanta.2017.06.027.

[34] Yang, J.Y., Yang, T., Wang, X.Y., Wang, Y.T., Liu, M.X., Chen, M.L., et al., 2019. A novel three-dimensional nanosensing array for the discrimination of sulfur-containing species and sulfur bacteria. Anal Chem 91 (9), 6012–6018. https://doi.org/10.1021/acs.analchem.9b00476.

[35] Zgagacz, W., Zakrzewski, R., Urbaniak, K., Chwatko, G., Nowicki, A., 2020. The use of high-performance liquid chromatography with diode array detector for the determination of sulfide ions in human urine samples using pyrylium salts. J Chromatogr B 1157, p. 122309. Available from: https://doi.org/10.1016/j.jchromb.2020.122309.

[36] Zhang, T., Liu, Y., Pi, J., Lu, N., Zhang, R., Chen, W., et al., 2022. A novel artificial peroxisome candidate based on nanozyme with excellent catalytic performance for biosensing. Biosens Bioelectron 196, 113686. https://doi.org/10.1016/j.bios.2021.113686.

[37] Zhang, W., Hu, S., Yin, J.J., He, W., Lu, W., Ma, M., et al., 2016. Prussian blue nanoparticles as multienzyme mimetics and reactive oxygen species scavengers. J Am Chem Soc 138 (18), 5860–5865. https://doi.org/10.1021/jacs.5b12070.
[38] Zhang, X.P., Huang, K.Y., He, S.B., Peng, H.P., Xia, X.H., Chen, W., et al., 2021. Single gold nanocluster probe-based fluorescent sensor array for heavy metal ion discrimination. J Hazard Mater 405, 124259. https://doi.org/10.1016/j.jhazmat.2020.124259.
[39] Zhang, Z.H., Zhang, S.D., Jiang, C.J., Guo, H.C., Qu, F.D., Shimakawa, Y., et al., 2021. Integrated sensing array of the perovskite-type LnFeO(3) (Ln(=)La, Pr, Nd, Sm(=)La, Pr, Nd, Sm) to discriminate detection of volatile sulfur compounds. J Hazard Mater 413, 125380. https://doi.org/10.1016/j.jhazmat.2021.125380.
[40] Zhu, X., Tang, J., Ouyang, X., Liao, Y., Feng, H., Yu, J., et al., 2022. Multifunctional MnCo@C yolk-shell nanozymes with smartphone platform for rapid colorimetric analysis of total antioxidant capacity and phenolic compounds. Biosens Bioelectron 216, 114652. https://doi.org/10.1016/j.bios.2022.114652.
[41] Zhu, Y., Wu, J., Han, L., Wang, X., Li, W., Guo, H., et al., 2020. Nanozyme sensor arrays based on heteroatom-doped graphene for detecting pesticides. Anal Chem 92 (11), 7444–7452. https://doi.org/10.1021/acs.analchem.9b05110.